ORIGINAL PAPER

In-Situ FTIR and Laser Induced Fluorescence RONS Characterization of Atmospheric Pressure Nanosecond-Pulsed Surface DBD Plasma for Indirect Treatments of *E. Coli*

Lorenzo Ibba[1] · Rita Agus[1] · Fabio Avino[1] · Ivo Furno[1] · Paolo F. Ambrico[2]

Abstract

We study the bactericidal efficacy of surface dielectric barrier discharge low-temperature plasma treatments, powered by nanosecond high voltage pulses. We achieve ~4-log reduction in *Escherichia coli* population, after 10 min treatments, at a distance of 1.5 cm from the plasma surface. To investigate the reactive oxygen and nitrogen species (RONS) responsible for the bactericidal effect, we employ in-situ fourier transform infrared (FTIR) spectroscopy to measure a selection of relevant species, such as O_3, NO_2, N_2O and N_2O_5. The measurements are taken under various relative humidity conditions to replicate the bacteria treatment environment. While RONS originating from nitrogen chemistry are detected, nitric oxide (NO), a pivotal molecule in nitrate production, is absent due to the sensitivity limitations of FTIR detection. To overcome this limitation, we employ laser induced fluorescence utilizing a picosecond-pulsed laser to measure the kinetics of NO produced by the plasma. Our results show that the NO concentration is smaller than 1 ppm and primarily localized near the plasma surface, with concentrations increasing proportionally with relative humidity. Notably, at a distance of 1.5 cm from the plasma surface, at which the *E. coli* is treated, the concentration of NO falls below 50 ppb. Although NO is pivotal in generating secondary reactive species within the plasma, our results suggest that it does not directly contribute to the bacteria inactivation process. Instead, other molecules, such as O_3, NO_2, and N_2O, which are found in higher concentrations, may be responsible for the bactericidal properties observed in indirect plasma treatments.

Keywords Plasma sterilization · Low-temperature plasmas · Laser induced fluorescence · In-situ FTIR spectroscopy · Nanosecond-pulsed plasmas · Dielectric barrier discharge

✉ Lorenzo Ibba
  lorenzo.ibba@epfl.ch

1 Ecole Polytechnique Fédérale de Lausanne (EPFL), Swiss Plasma Center (SPC), CH-1015 Lausanne, Switzerland

2 CNR, Istituto per la Scienza e Tecnologia dei Plasmi, Sede di Bari, Via Amendola 122/D, Bari, Italy

Springer

Introduction

Low-temperature plasmas (LTPs) at atmospheric pressure have been extensively investigated during the past decade for various biological applications [1], and recently they have attracted significant attention for their potential in decontamination and disinfection applications, with the objective to achieve sterilization [2–5]. Today, autoclaves are the workhorse of sterilization facilities, which reprocess the utensils, reagents, and wastes, indispensable for research in life sciences. They run constantly throughout the day to meet the demands of the research laboratories. Unfortunately, not only can a large autoclave consume several hundred liters of water (in wet heat treatment) in just one sterilization cycle, leaving an enormous environmental footprint, but it also consumes massive amounts of energy in the process [6]. In comparison with autoclaving, LTP-based sterilization techniques may offer several benefits, including lower energy consumption, lower temperature requirements, no need for high pressure or vacuum conditions, short treatment times, and no long-lived harmful chemicals. Thanks to these advantages, LTP sterilization offer an effective solution for addressing the sterilization needs of thermo-sensitive materials, which are currently not suitable for autoclave sterilization. Although LTPs hold out great promise for novel sterilization techniques, a comprehensive understanding of both the physics and biological aspects is essential prior to the commercialization and scaling-up of this technology.

To advance the research in LTP-based sterilization techniques, multiple device configurations have been tested: from plasma jets [7, 8], where a LTP is blown to a localized area by a gas flow, to volume and surface dielectric barrier discharges (VDBD and SDBD) [9–11], where a LTP is generated within a volume or over a surface. Depending on the device configuration and the position of the biological target with respect to the plasma, the treatment is defined direct or indirect. If the target is in contact with the plasma the treatment is referred to as "direct", while if it is not in contact with the plasma, but close enough for by-products of the plasma to reach the target, then the treatment is called "indirect". Plasma jets and VDBDs are used in direct plasma treatments while SDBDs in indirect plasma treatments. Direct plasma treatments are in most cases faster [12], however, indirect plasma treatments are still proven effective with the advantage of simpler deployment [13]. In both cases the plasma produces ions, electrons, reactive oxygen and nitrogen species (RONS), UV radiation and electric fields, whose sinergy is believed to be the cause behind bacteria inactivation by LTPs. RONS play a critical role in the process [14], especially in indirect plasma treatments where the target is far from the plasma and only by-products, such as long-lived RONS, can reach it. Among the RONS generated by LTPs, ozone (O_3) stands out as a well-known antimicrobial molecule, as indicated by various studies [15–17]. The bactericidal effects of ozone have been extensively explored for different applications, including treatments on both dry and wet surfaces [18, 19], food decontamination [17], and bacteria bio-film inactivation [20]. Previous research has established a connection between ozone and bactericidal efficacy, with findings suggesting that ozone is a primary reactive species produced by LTPs in similar configurations, playing a crucial role in bacteria inactivation [21]. However, it is noteworthy that NO_x (nitrogen oxides) products also contribute significantly to the bacteria inactivation process during SDBD indirect plasma treatments, as evidenced in prior studies [22]. A pivotal molecule in this context, not only for its bactericidal properties but also as a precursor to other NO_x molecules, is nitric oxide (NO) [23, 24]. Although simulations suggest that NO concentration is minimal in the region adjacent to the plasma [25], experimental data on NO concentration and its kinetics are scarce in

SDBD configurations. Previous studies of NO in SDBD plasmas have primarily relied on average measurements, which do not provide information on the concentration at specific distances from the plasma source or at specific time intervals between discharges [26, 27]. Thus, the current understanding of RONS produced by SDBDs is incomplete, particularly with respect to the influence of critical parameters such as power, applied voltage, relative humidity, and distance from the plasma surface.

To address this knowledge gap, we present a study of relevant RONS produced by an SDBD plasma operating at atmospheric pressure, using in-situ fourier transform infrared (FTIR) spectroscopy measurements. Additionally, we measure the NO concentration via picosecond laser induced fluorescence (LIF), with a focus on the impact of plasma discharge power, frequency, relative humidity, and distance from the plasma surface. These measurements allow for a better understanding of the role of NO and other species in the decontamination process by indirect plasma treatments. Special emphasis has been placed on maintaining consistent conditions, including factors such as relative humidity (RH), flow rate, and proximity to the plasma source, during the bacterial treatments as well as in both FTIR and LIF measurements.

Materials and Methods

### Nanosecond-pulsed Surface DBD

The plasma discharge is produced using a SDBD powered by a custom-made nanosecond-pulsed high voltage power supply, able to generate monopolar pulses as short as 200 ns, up to 25 kV peak, at 100 to 2000 Hz frequency. In this work, if not stated otherwise, we use 4.7 kV and 400 ns long pulses, at 1 kHz repetition frequency, as shown in Fig. 1.

The SDBD is a printed circuit board (PCB) developed specifically for this application. The SDBD has a round geometry of 74 mm diameter (Fig. 2a) to fit inside a standard petri dish of 90 mm diameter. The 0.3 mm thick dielectric is FR4 (Flame Retardant 4) while the electrodes are 0.1 mm-thick Cu plating, treated with electroless nickel
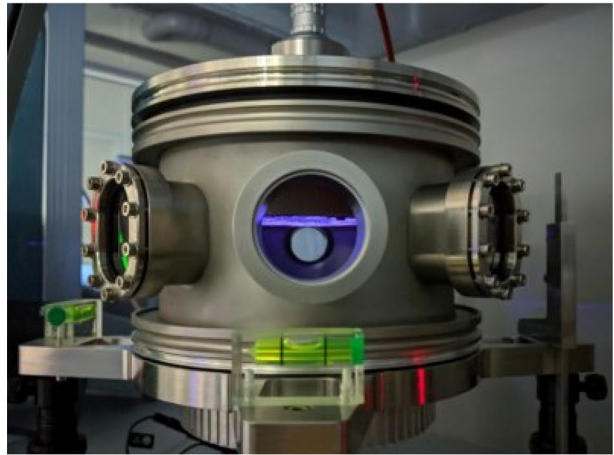

Fig. 1 Voltage pulse waveform in kV and plasma emission in arbitrary units, showing the two plasma discharges in correspondence of the rising and falling edge of the voltage pulse
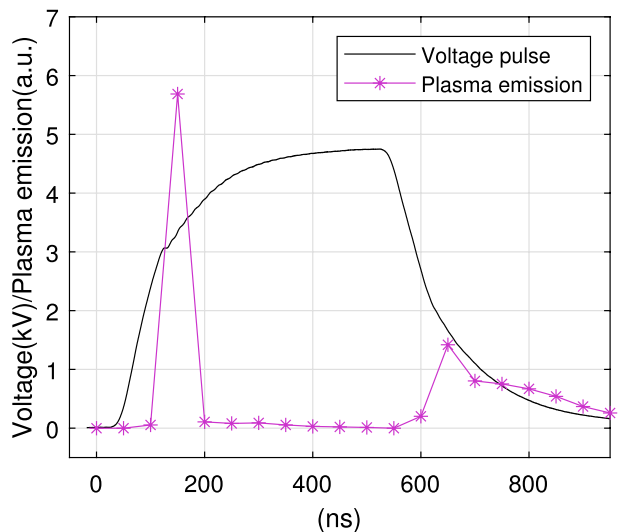
Fig. 2 Picture of operating SDBD with visibile multi-finger configuration (**a**) and of SDBD operating inside the reactor (**b**)
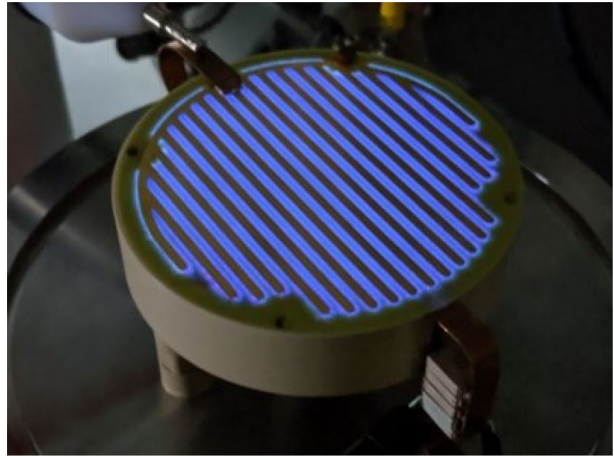
(a)

(b)

immersion gold (ENIG), resulting in a nickel plating to facilitate soldering, and a gold film coating intended to protect the copper electrodes against oxidation and corrosion. The high-voltage electrode is an array of flat fingers, each measuring 2 mm in width and spaced 2 mm apart. In contrast, the ground electrode on the opposite side is a solid flat plate. The multi-finger configuration of the substrate-exposed high-voltage electrode is chosen to have an homogenous plasma distribution over the Petri dish surface. The SDBD is placed upside down within a sealed stainless steel cylindrical reactor (Fig. 2b) of 15 cm internal diameter and a volume of approximately 2 ls.

The reactor features eight lateral flanges that are symmetrically arranged to allow optical access to the plasma. Sapphire windows are positioned at 90-degree angles to allow the laser and fluorescence to enter and exit, respectively, the reactor, while keeping it sealed. On one flange the Vaisala HUMICAP HM42 probe [28] is installed to measure the relative humidity and temperature of the gas, whereas other two flanges allow for the inflow and outflow of the gas.

The gas flow is regulated by three Bronchorst mass flow controllers: one for pure nitrogen (N_2), one for pure oxygen (O_2), and one for dry synthetic air. The humid synthetic air is generated through the bubbling of dry synthetic air in deionized water. We use dedicated Bronkhorst gas-mixing junction/T-components to optimize the mixing of gases with significantly different flow rates. This method of producing humid synthetic air ensures a highly controlled and reproducible level of humidity in the gas mixture. The proportion of nitrogen to oxygen in the gas mixture is maintained at a ratio of 4:1, while the total flow rate is kept constant at 3000 sccm, with a passive exhaust. This methodology effectively minimizes the influence of flow rate variation and enables the precise assessment of changes in relative humidity. Three distinct flow configurations are investigated in this study:

- RH $\simeq$ 0%: 0 sccm humid synthetic air, 2400 sccm N_2, 600 sccm O_2.
- RH = 13% $\pm$ 2%: 500 sccm humid synthetic air, 2000 sccm N_2, 500 sccm O_2.
- RH = 23% $\pm$ 2%: 1000 sccm humid synthetic air, 1600 sccm N_2, 400 sccm O_2.

These three experimental conditions will be referred to as 0% RH, 13% RH and 23% RH. The RH fluctuations are caused by the slight increase in temperature ($< 10\,°C$) of the gas and by the operation of the plasma discharge.

The plasma discharge power is assessed using Lissajous figures [29, 30]. This approach provides a reliable means of measuring the plasma discharge power in DBD plasma sources and it has been widely adopted in plasma research. A monitor capacitor is placed in series with the SDBD, on the ground side of the circuit. The transferred charge $Q(t)$ on the monitor capacitor is obtained through $Q(t) = C_m V_m(t)$, where $V_m(t)$ is the voltage measured across the monitor capacitor and C_m its capacitance. The energy per pulse is then computed integrating the voltage applied to the SDBD $V(t)$ over the transferred charge $Q(t)$: $E_{pulse} = \oint V(t)dQ(t)$. This value is graphically represented by the area enclosed by the $Q - V$ plot, also called Lissajous figure, as depicted in Fig. 3a. To obtain the average power dissipated by the plasma discharge the energy per pulse is multiplied by the frequency $\overline{P} = E_{pulse}f$.

The fast rise time of the nanosecond voltage pulse results in stray capacitance and noise on the $V_m(t)$ and $V(t)$ signals, necessitating meticulous attention to circuit design, including cable length reduction to minimize circuit loops. Furthermore, the synchronization of signals at the nanosecond level is a challenging task and can cause significant measurement errors. To address this, the delay between the probes has been measured, and the signals have been shifted accordingly to improve the synchronization. The uncertainty on the delay between the probes, approximately 2 ns, translates in an error on the plasma discharge power, represented by the shaded area in Fig. 3b. The voltage on the capacitor is measured using a standard 10:1 attenuation voltage probe (Tektronix TPP0201), while the voltage on the SDBD is measured using a 1000:1 attenuation high voltage probe (PMK PHV 4002-3). The signals are acquired by a Teledyne Lecroy oscilloscope (Lecroy HDO LCRY3502N04187). As shown in Fig. 3a, the obtained Lissajous figures are similar to those reported in [31] for a nanosecond-pulsed SDBD plasma. The power used for the bacteria treatments and the FTIR and LIF measurements is ~1.3 W, at 4.7 kV. Assuming the surface covered by the plasma is half the SDBD area $8^2\pi/2 \sim 100$ cm^2, the surface power density is ~0.013 W/cm^2, which is significantly lower than the ~0.1 W/cm^2 threshold value found in [32] separating the so-called ozone-mode from the nitrogen oxides-mode [22]. We thus expect the ozone production to be dominant with respect to the nitrogen oxides products in the present experiments. Additionally, the temperature of the substrate-exposed surface of the DBD was measured using a thermal camera (Teledyne FLIR E85). At an

Fig. 3 **a** Lissajous figures at increasing applied voltages, namely 2.1 kV, 4.7 kV and 5.7 kV. **b** Plasma discharge power at increasing applied voltages. The shaded area represents the error associated with the uncertainty on the synchronization of the signals
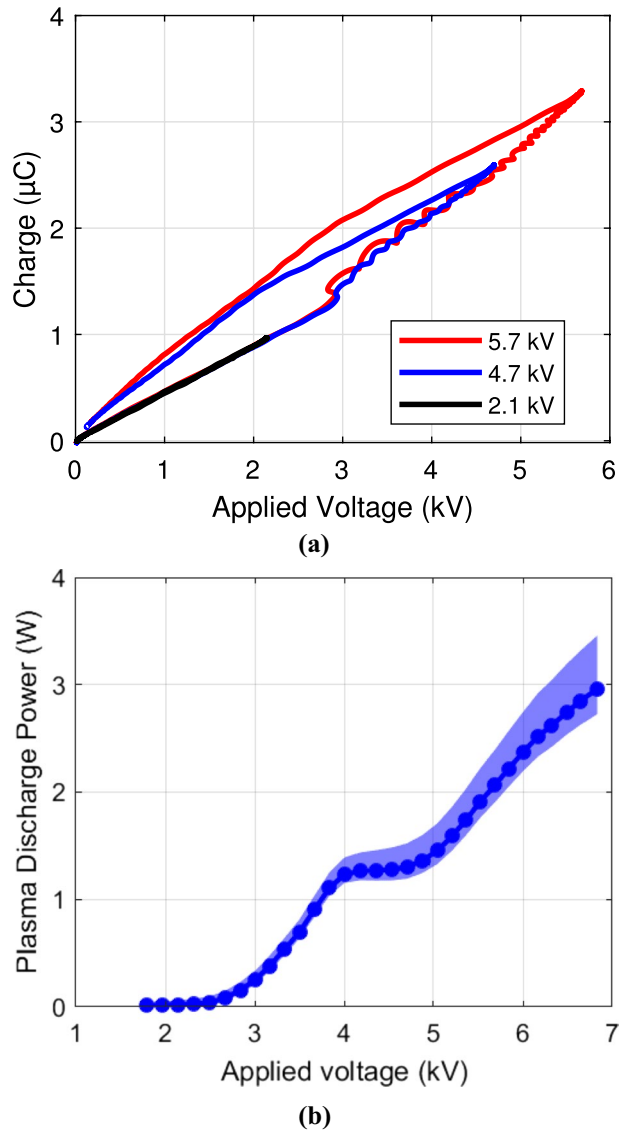
applied voltage of 4.7 kV, the maximum temperature of the DBD surface is approximately 27 °C. Increasing the applied voltage to 6.8 kV, and consequently increasing the dissipated power, led to a temperature rise of approximately 13 °C, deemed irrelevant for the conclusions of this work.

E. coli Culture Management and Plasma Treatment Protocol

Non pathogenic *Escherichia coli* K-12 strain MG1655 is used to test the decontamination efficacy of plasma treatments with this setup. 100 µL of the bacterial cell stock,

preserved in a solution of Lysogeny Broth (LB) and glycerol (30% v/v) at a temperature of $-80\,°C$, are inoculated into 10 mL of LB and then incubated at $37\,°C$ and 180 rpm for a minimum of 8 h, to produce the overnight culture. To reactivate the bacteria culture, 10μL of the overnight culture are inoculated into 10 mL of fresh LB and incubated at $37\,°C$ and 180 rpm. To assess the growth phase of the cells, the optical density (OD) at 600 nm is measured. The bacteria are treated during the mid-log phase, which is characterized by favorable environmental conditions for bacteria replication. This phase corresponds to an OD between 0.2 and 0.3, indicating a concentration of approximately 10^6 colony-forming units per milliliter (CFU/mL) [33, 34].

From the culture, 5 serial dilutions are obtained and plated in standard petri dish filled with agar. For each treatment time, all the 5 dilutions and the undiluted are treated with the same protocol inside the reactor. After the treatments the bacteria are incubated at $37\,°C$ and 180 rpm for 24 h, after which the CFU/mL are counted. The results are plotted in logarithmic scale according to the following definition $\log_{10}(N_0/N)$, with N_0 being the initial bacteria population, counted on the control, and N the bacteria population after the plasma treatment. The log-reduction value shows the CFU/mL reduction after the plasma treatment. *E. coli* plasma treatments were performed in triplicates from 30 s to 10 min of continued plasma exposure, inside the reactor with the flow configuration 0% RH, as shown in Fig. 4.

The gas flow is controlled to have steady state conditions and avoid an increase in RH due to the water released by the agar plate. High levels of RH can lead to deterioration and/or damage of the SDBD [35]. This would prevent plasma ignition homogenously over the whole surface, leading to erroneous or misleading results. The RH is monitored during the treatments and it stabilizes at around 10–13%. The in-situ FTIR and LIF measurements are performed in the same RH and flow conditions to reproduce the same setup of the bacteria treatments.

Statistical Analysis

The statistical analysis was performed using the statistical program CoStat [36]. Analysis of variance (ANOVA) was used to compare different treatment times. Significant differences were identified by the Student-Newman-Keuls multiple range test [37, 38], with a confidence level at $p \leq 0.05$. Different lowercase letters, from a to c, indicate significant difference.

Fig. 4 Schematics of the *E. coli* plasma treatments with the SDBD inside the reactor
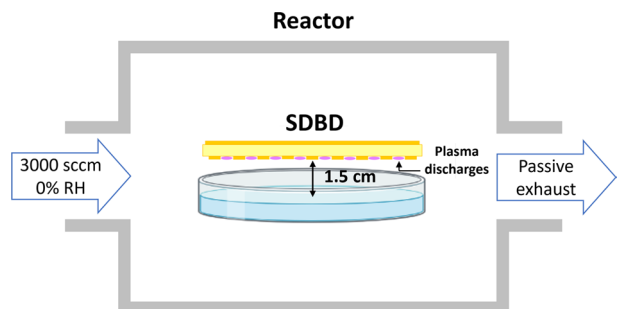
In-situ FTIR Experimental Setup

The FTIR measurements are performed in-situ using a Bruker Vertex 80v [39]. The reactor is placed inside the sample compartment of the Vertex 80v, with the IR beam passing ~ 1.5 cm in front of the plasma surface, as shown in Fig. 5, same distance at which *E. coli* is treated. To seal the reactor, two KBr windows, 30 mm diameter, are placed on the line of sight of the IR beam. The optics bench of the vacuum FTIR spectrometer is sealed, instead, by a 49.5 mm diameter ZnSe window on each side of the sample compartment. Because of the electrical connections and gas tubing to the reactor, the sample compartment remained open, hence the IR beam also traversed the ambient air outside of the reactor over a short distance, approximately 2 cm in total, causing fluctuations of CO_2 and H_2O concentration.

A single FTIR measurement is averaged over 16 s, allowing for 20 s time-steps single measurements. The FTIR spectra is acquired over 10 min of plasma operation, which is the longest bacteria treatment performed. The spectra are analyzed and compared to reference spectra of specific gases, namely O_3, NO_2, N_2O, N_2O_5 and HNO_3.

The absolute calibration of the IR signal is performed using the Beer-Lambert law [40]. The concentration in ppm of a specific molecule is given by:

$$n_i = \frac{A(v)}{\sigma_i(v)L}\left(\frac{10^{12}}{n}\right) \tag{1}$$

where $A(v) = \ln(I_0/I)$ is the absorbance as a function of wavenumber v, with I_0 being the radiant power of incident light on the sample and I the radiant power transmitted by the sample. Since the spectrometer absorbance measurement is defined as $A(v) = \log(I_0/I)$, a correction factor equal to ln 10 must be taken into account. $\sigma_i(v)$ is the absorption cross-section of species i as a function of v in $cm^2 molecule^{-1}$, L is the length of the absorbance pathway in cm. The last term $10^{12}/n$ is a conversion factor needed to pass from molecule/cm^3 to ppm, with n being the density of the gas, in our case air at room temperature and atmospheric pressure. The absorption cross-section values for particular molecules, such as O_3, NO_2, N_2O are obtained from the HITRAN database [41], with the exception of N_2O_5, for which only the relative concentration is reported.

Nitric Oxide LIF Experimental Setup

LIF measurements are performed using a diode-pumped high energy picosecond Nd:YAG laser (PL2231-50 Ekspla [42]) to excite NO at 226.1 nm wavelength with a

Fig. 5 Schematic of the in-situ FTIR measurements setup
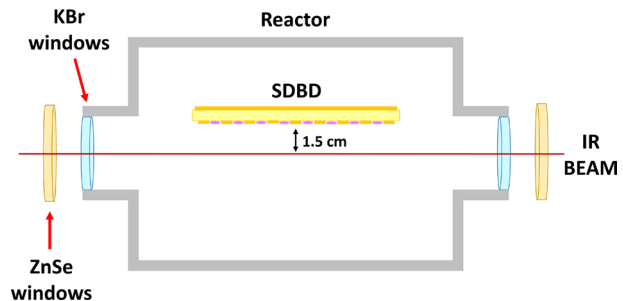
pulse duration (FWHM) of 28 ps $\pm$ 10%, at 50 Hz repetition rate. The optical setup for the LIF measurements is detailed in Fig. 6.

To detect the fluorescence we use a gated ICCD (PM4-1024f-RB-PS-18-P43 by Teledyne Princton Instruments [43]) with ~12% quantum efficiency in the UV. In front of the ICCD, we position a 248 nm long-pass filter to eliminate any scattered light originating from the laser beam. Additionally, we use a 257/12 nm band-pass filter to selectively capture the emission band of NO (X $^2\Pi$, v=3) at around 257 nm. To collect the fluorescence, we employ two UV fused silica plano-convex lenses with a focal length $f = 300$ mm. The laser beam is focused inside the reactor using the same plano-convex lens. To monitor the synchronization between the ICCD, the laser pulse, and the plasma discharge, a photodiode (DET10A2 by Thorlabs) is placed in front of the focusing lens reflection. The energy of the beam is measured and monitored in real time with a pyroelectric detector (QE8SP-B-MT-D0 by Gentec-eo) to be approximately ~40μJ. This particular energy level for the laser pulse is chosen to minimize noise caused by scattered light within the reactor and to maximize the signal-to-noise ratio.

We conducted a scan of the LIF signal, while gradually increasing the laser pulse energy, ensuring that we remained below the saturation regime. The data in Fig. 7 clearly demonstrates that we are operating comfortably within the linear regime. The synchronization between the plasma discharge, the ICCD and the laser is controlled by the nanosecond-pulsed power supply. The control system, made with a cRIO-9063, generates a TTL trigger which is fed to the laser. In turn, a TTL generated by the laser, triggers the ICCD for the gate synchronization. The relative position between the plasma surface and the laser beam is controlled with a motorized vertical translation stage (Thorlabs MLJ150/M) and an horizontal micrometer translation stage, to be able to accurately reconstruct a 2D image of the LIF measurements over a 4x4 mm area as shown in Fig. 8. The laser beam is parallel to the electrode fingers so to preserve the symmetry along the laser beam path and the beam width is ~1 mm.
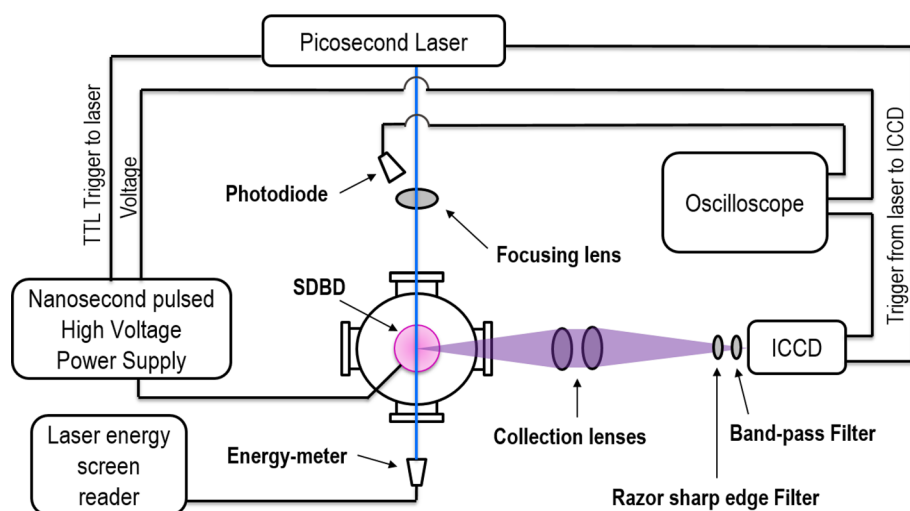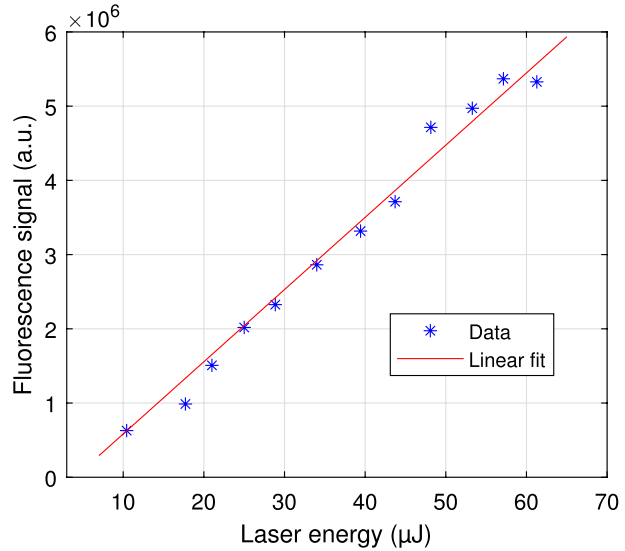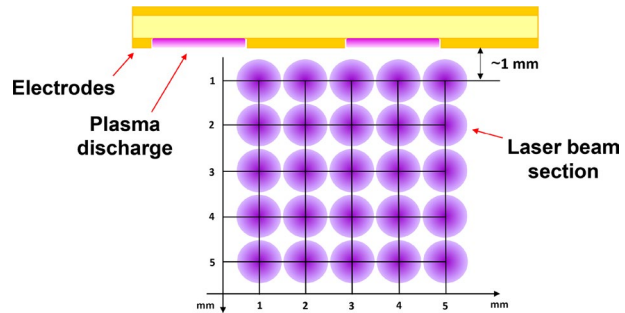

Fig. 6 LIF experimental setup schematics

Fig. 7 LIF signal in arbitrary units at increasing laser pulse energy and linear fit of the data

Fig. 8 Vertical section of the experimental setup showing the relative position between the laser beam and the SDBD plasma for the 2D LIF measurements

Nitric Oxide LIF Theory

The time-integrated LIF signal $I(\lambda)$, as a function of the excitation wavelength λ, is a sum over all the rotational transitions i with wavelength λ_i exited by the laser wavelength λ [44],

$$I(\lambda) = ClE\frac{A_{det}}{A_{tot} + Q}n \sum_i B_i f_i \Gamma(\lambda - \lambda_i), \tag{2}$$

where C is a constant to take into account the efficiency of the detection system and the collecting optics; l is the length of the detection volume along the laser beam; E is the energy of the laser pulse; A_{det} is the Einstein emission coefficient of the NO A($v = 0$) → X($v = 3$) fluorescence transition which is measured by the detection system; A_{tot} is the total emission coefficient of the NO A($v = 0$) state; Q is the quenching rate of the NO A($v = 0$) state, which depends on the gas temperature and composition; n is the density of the NO X($v = 0$) ground state; B_i is the Einstein absorption coefficient of the transition i; $f_i(T_{rot})$ is the Boltzmann factor of the rotational state of transition i, dependent on the rotational temperature T_{rot}; Γ is the normalized line profile. The derivation of Eq. (2) is described in

detail in [44], and a similar one is used in [45]. With a temperature variation between 300 K and 600 K [46], such that in the experiments herein, the sum over the rotational transitions does not vary significantly, hence the term

$$ClEA_{det} \sum_i B_i f_i \Gamma(\lambda - \lambda_i)$$

(3)

is constant for the plasma discharge measurement and the calibration. Time resolved measurements of the LIF are taken to measure the quenching rate Q of the exited state of NO (A $^2\Sigma$). The gate time of the ICCD is chosen to be 5 ns and delayed with respect to the laser pulse at 1 ns timesteps. Longer gate times did not improve the measurements, and shorter than 1 ns were insufficient to detect the fluorescence signal. The fluorescence decay is then fitted with an exponential function e^{kt+b}, where $k = A_{tot} + Q = \tau^{-1}$ is the time decay constant of the fluorescence.

In Fig. 9 is shown an example of the time resolved fluorescence decay, and the fitting exponential function used to measure the quenching rate Q. To determine the absolute density n from the time-integrated LIF signal I, the experimental setup requires calibration with a gas mixture containing a known density of NO. This calibration is performed by injecting 0.5, 0.6, 0.7, 0.8 and 0.9 ppm of NO in the reactor and measuring the LIF signal emitted. The data is then fitted, as shown in Fig. 10, and the calibration constant extrapolated.

The difference in the quenching of the LIF signal between the calibration and plasma measurement is corrected by taking into account the decay time τ. Fluctuations in the laser power are accounted for by measuring the laser energy E. The absolute density n of the NO X($v = 0$) ground state can then be calculated as:

$$n = \frac{n_{cal} E_{cal} \tau_{cal}}{I_{cal}} \frac{I}{E\tau}$$

(4)

where the subscript *cal* indicates the quantities obtained in the calibration.

Fig. 9 Example of a time resolved raw data set of the LIF signal, showing the fluorescence decay timing, and the exponential fit used to infer the quenching rate Q
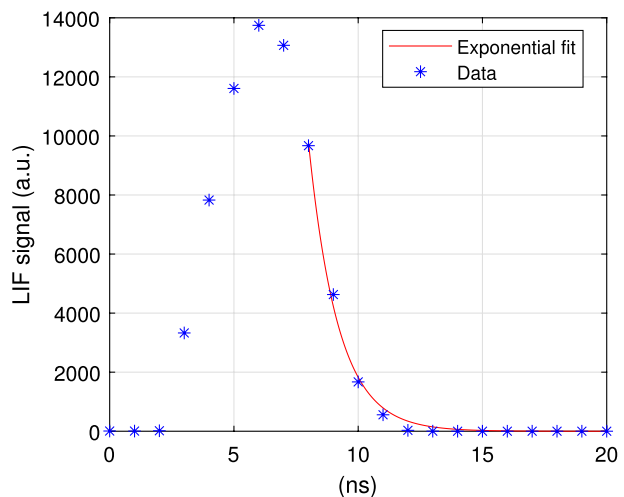
Fig. 10 LIF signal emitted by different concentrations of NO for absolute calibration. Raw data and linear fit are shown in the plot
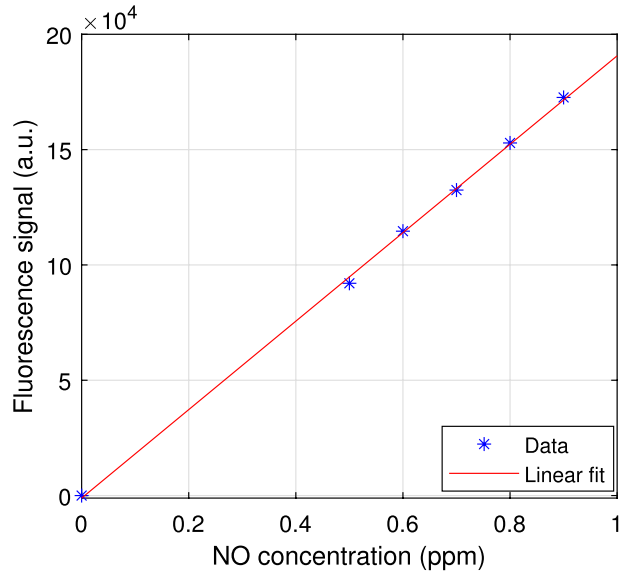

Results and Discussion

E. coli Plasma Treatments

The plasma treatments of *E. coli* are performed in triplicates for each treatment time. The plot in Fig. 11 shows the mean and standard deviation of the CFUs log-reduction of *E. coli* for increasing plasma treatments time. Bacteria population is reduced by 4-log after 10 min of plasma exposure.

Fig. 11 Log reduction of *E. coli* depending on the duration of plasma exposure. Mean and standard deviation of triplicates are represented. Different lower-case letters indicate significant differences ($p \leq 0.05$)
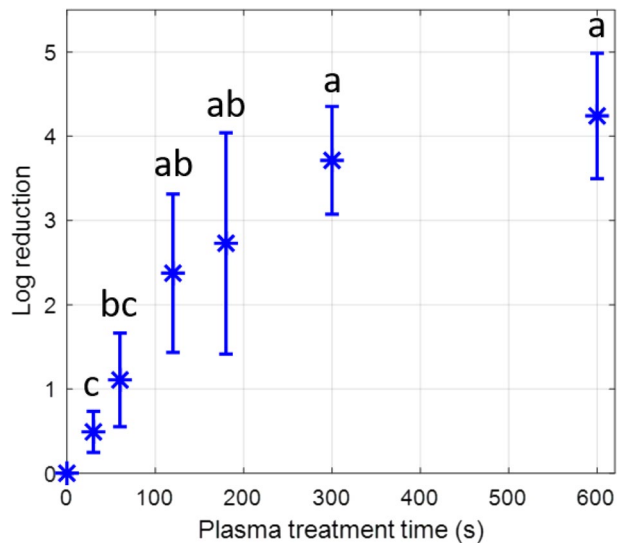
The gas flow, perpendicular with respect to the plasma surface, did not affect significantly the disinfection efficacy of the treatments. To evaluate the isolated impact of nitric oxide on bacteria, *E. coli* was subjected to a 10-minute treatment of 1 ppm of NO in a 3000 sccm synthetic air flow, the same setup used for the plasma treatments. The nitric oxide treatments, carried out in triplicates, demonstrated that the exposure to 1 ppm of NO did not yield any discernible effect on the bacteria population.

In-situ FTIR Measurements

FTIR spectra were measured at a temporal resolution of 20 s for 10 min after the initiation of the plasma discharge, for the three distinct flow configurations.

Figure 12 presents a series of spectra obtained for the 0% RH flow setup, wherein the background spectrum, at t = 0 s, was acquired prior to the initiation of the plasma discharge. A strong absorption peak at approximately 1352 cm^{-1} is caused by an irreversible surface transformation of the KBr windows, probably KNO_3 [47], due to a reaction of the NOx species produced in the plasma with the KBr windows [48]. The characteristic peaks of N_2O, NO_2, N_2O_5, and O_3 are distinctly observed. Nonetheless, the measured spectra did not exhibit any discernible signal for NO due to its insufficient concentration for the FTIR to be detected. The Bruker Vertex 80V detection limit for NO falls below 10 ppm, as confirmed by injecting 1 to 10 ppm NO inside the reactor. The characteristic peak of HNO_3 is around 1720 cm^{-1}, overlying the main peak of N_2O_5 at the same wavelength. However, all the bands of N_2O_5 are present, at 743, 1246 and 1720 cm^{-1} [49]. On the contrary, secondary peaks of HNO_3 are absent, suggesting the peak at 1720 cm^{-1} is entirely N_2O_5.

Figure 13 shows the time evolution of the concentration in ppm of O_3, N_2O and NO_2, and the relative concentration of N_2O_5. As expected, the Ozone concentration is much higher with respect to the other species, since the SDBD is operated at a low surface power density. The trends show clear correlations of the aforementioned species dynamics, with respect to the RH. Ozone, N_2O and N_2O_5 decrease with increasing RH, while NO_2 follows the opposite trend. However, there is no significant difference between 13% RH and 23% RH, in the case of NO_2, as well as in between 0% RH and 13% RH, in the case of N_2O_5. It is also important to notice that while O_3 and N_2O, after an initial build-up phase, reach a
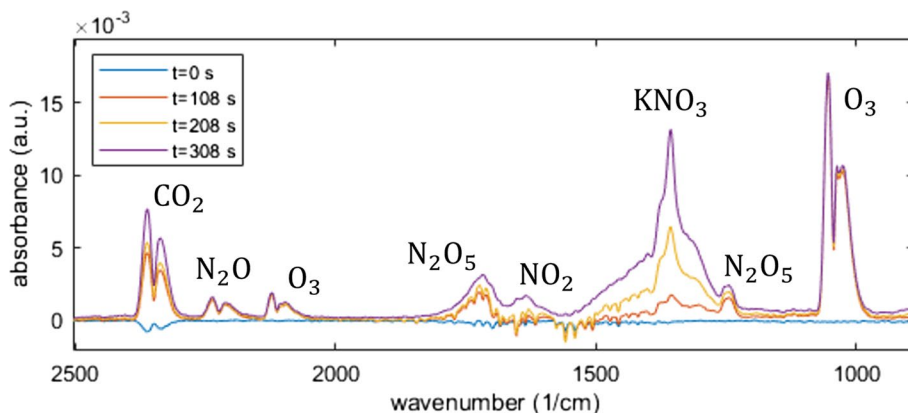
Fig. 12 In-situ FTIR absorption spectra at 0% RH acquired at different time intervals from plasma start. The plot is trimmed to exclude non-relevant wavenumbers
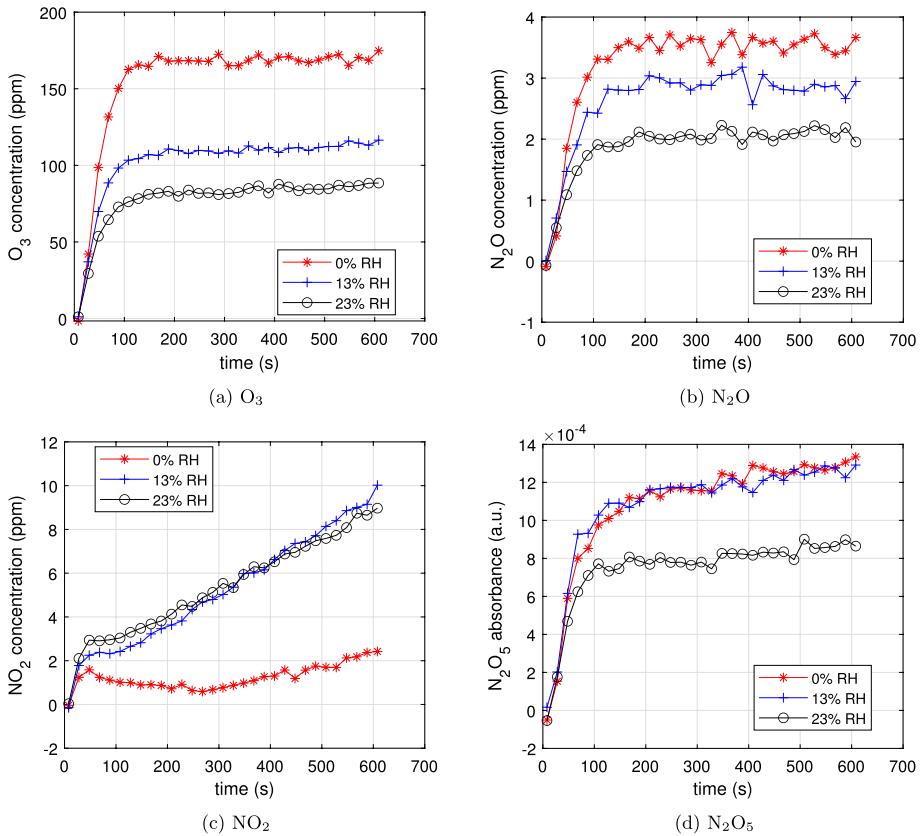
Fig. 13 10 min evolution of the concentration of O_3, N_2O, NO_2 in ppm and N_2O_5 in arbitrary units obtained from FTIR absorption spectra. The measurements for the 3 different flow configurations are reported

dynamic equilibrium, N_2O_5 and especially NO_2 keep increasing with a linear trend. This behavior suggests that 3000 sccm flow intensity is not enough, in this setup, to reach a dynamic equilibrium for all the species. It is possible that NO_2 keeps increasing by depleting N_2O and O_3.

Nitric Oxide LIF Measurements

LIF measurements to study the time evolution of NO concentration are conducted in a fixed position, closest to the plasma ignition area, in between the electrodes, approximately 1 mm from the DBD surface. Figure 14 shows the NO concentration in ppm at different delays from the plasma discharge, every 100 µs time-steps, at 0% RH, 13% RH and 23% RH.

The error bar represents the standard deviation resulting from the exponential fit of the fluorescence decay, attributed to slight variations observed during the individual measurement, which lasted over 6 min. The variations of RH and other quenchers, particularly in the vicinity of the plasma region, lead to slightly different decay times and consequently introduce errors in the measured concentrations. As depicted in Fig. 14, the NO concentration exhibits an increase with larger RH. However, it is stable over time, in between

Fig. 14 NO concentration between plasma discharges at 1 kHz frequency, 1 mm from the DBD surface, at 0% RH, 13% RH and 23% RH
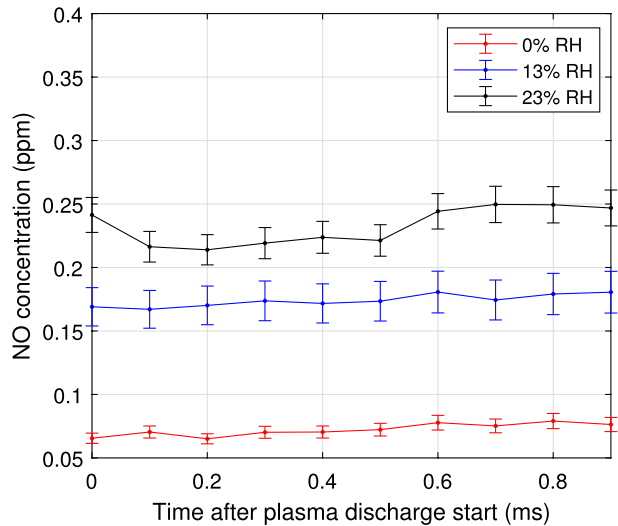
plasma discharges, throughout the operation of the SDBD. For the 2D reconstructions, measurements were taken 500 µs after the plasma discharge, as the concentration remains stable over time. This selection represents the midpoint between plasma discharges. The measurements shown in Fig. 15 reveal that the NO concentration follows the pattern of the electrodes, localized near the plasma and diffusing from the plasma surface. It rapidly decreases a few millimeters away from the plasma surface, and at a distance of 1.5 cm, where bacteria are treated, the concentration is approximately 50 ppb, as shown in Fig. 16.

To gain a better understanding of NO production by atmospheric pressure LTP, measurements of NO concentration were conducted at different plasma discharge powers by altering the voltage applied to the SDBD, as shown in Fig. 17. The results indicate that the NO concentration increases with increasing power at 13% RH and 23% RH, while it stays constant at 0% RH. At 23% RH value, an increase in NO production occurs even at lower power. To further confirm the correlation between NO production and plasma discharge power, the measurements were repeated at a frequency of 100 Hz, with the power reduced by a factor of 10 while maintaining the voltage at 4.7 kV.

The concentration of NO, as demonstrated in Fig. 18, follows a similar trend with respect to RH but is higher at lower frequency. The frequency between discharges exhibits a notable influence on NO concentration, indicating that the correlation with power is not straightforward. Temperature is another factor that has a significant impact on the production of NO [46]. However, the gas temperature rose by less than 10 °C during the operation, and at lower frequencies, the temperature increased proved to be even more negligible. This suggests that such minor temperature fluctuations cannot be considered a substantial influencing factor on the concentration of NO in this particular case.

Conclusions

In this study, we present the first 2D spatially and time-resolved picosecond LIF measurements of nitric oxide concentration produced by a nanosecond-pulsed SDBD plasma. Our measurements show a low (<1 ppm), yet stable concentration of nitric oxide over time. The

Fig. 15 NO concentration in ppm over a 2D 4 × 4 mm area, perpendicular to the DBD surface, at 0% RH (**a**), 13% RH (**b**) and 23% RH (**c**)

(a) 0% RH

(b) 13% RH

(c) 23% RH
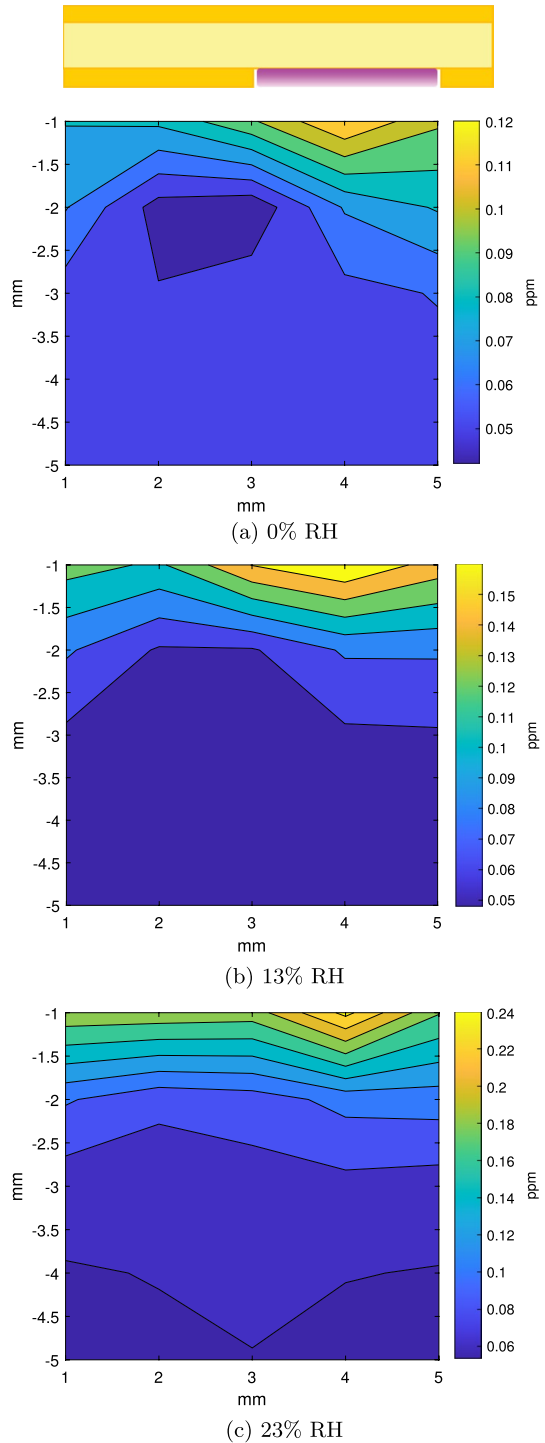
Fig. 16 NO concentration between plasma discharges at increasing distance from the plasma surface, at 0% RH, 13% RH and 23% RH
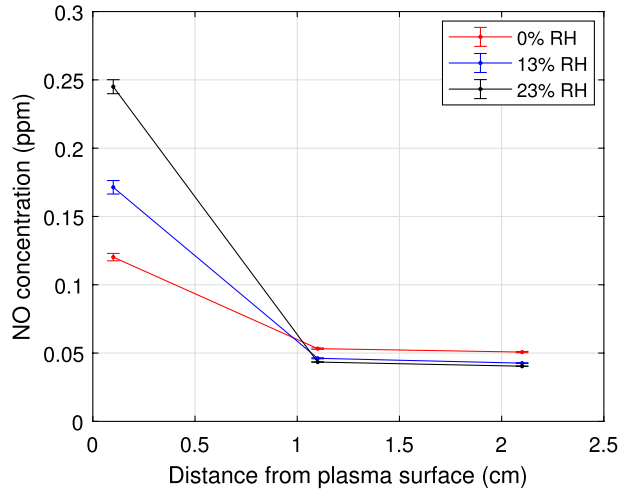

Fig. 17 NO concentration between plasma discharges at increasing plasma discharge power, 1 mm from the DBD surface, at 0% RH, 13% RH and 23% RH. The measured NO concentration is reported for increasing plasma discharge power obtained varying the applied voltage to the SDBD at 2.7, 3.5, 4.4, 5.2, 6.0, 6.8 kV
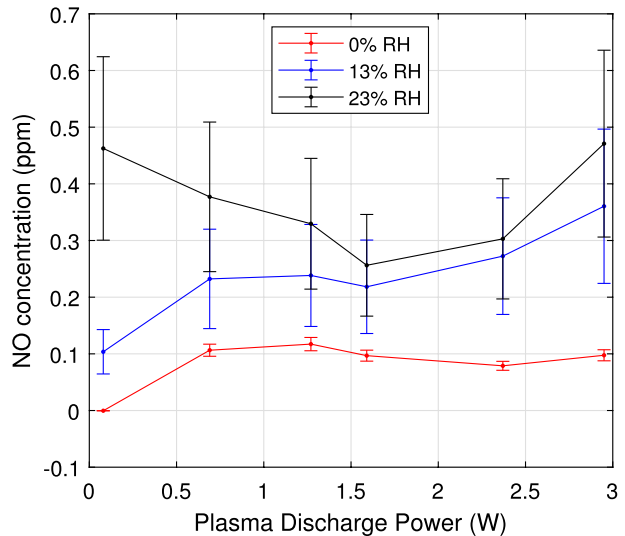
results are consistent with the NO concentration predicted by kinetic models [25], as the diffusion time of NO is slower than its decay time. However, we observe a notable increase in NO concentration in the vicinity of the plasma surface. The NO production also increases with plasma discharge power, but a non trivial correlation with power was found in this work, since lower frequencies yield higher NO concentrations at the same RH conditions. Furthermore, our findings establish a clear link between NO production and relative humidity, with higher RH values leading to increased NO concentrations. As we move farther away from the plasma surface the concentration of nitric oxide diminishes significantly. At a distance of 1.5 cm from the plasma surface, which corresponds to the location where the *E. coli* treatments are conducted, the measured NO concentration remains approximately 50 ppb. This concentration is notably lower than the suggested threshold of 160 ppm for effective antimicrobial action, as indicated by previous studies [50]. Indeed, this has been substantiated through treatments of *E.*

Fig. 18 NO concentration between plasma discharges at 100 Hz frequency, 1 mm from the DBD surface, at 0% RH, 13% RH and 23% RH. The applied voltage to the SDBD is 4.7 kV, resulting in a plasma discharge power of 0.13 W
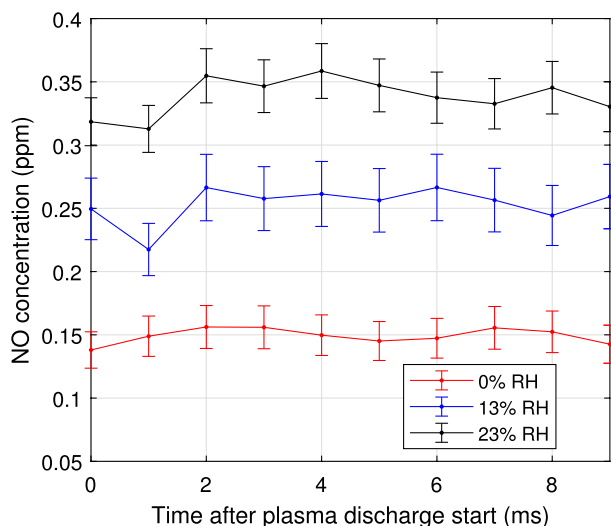
coli with 1 ppm of nitric oxide for 10 min, demonstrating no noticeable effect on the bacteria's survivability. Nonetheless, the observed substantial 4-log reduction in *E. coli* obtained through low-temperature plasma treatments suggests that other reactive species are contributing significantly to the inactivation mechanisms. In-situ FTIR measurements hint at the involvement of ozone (O_3) and by-products of NO, including NO_2, N_2O, and N_2O_5, in the bacterial inactivation process during indirect plasma treatments. However, further extensive investigations are essential to fully confirm and understand the role of these species in the inactivation process.

Data Availability The data used in the current study are available upon request to the corresponding author.

Declarations

Conflict of interest The authors declare no competing interests.

Ethical approval Not applicale.

References

1. Panariello BHD, Duarte S (2020) Comprehensive biomedical applications of low temperature plasmas. Arch Biochem Biophys. https://doi.org/10.1016/j.abb.2020.108560
2. Akikazu S, Yoshihito Y, Takashi O (2019) Disinfection and sterilization using plasma technology: fundamentals and future perspectives for biological applications. Int J Mol Sci. https://doi.org/10.3390/ijms2020 5216
3. Kostov KG et al (2010) Bacterial sterilization by a dielectric barrier discharge (DBD) in air. Surf Coat Technol. https://doi.org/10.1016/j.surfcoat.2010.01.052
4. Choi JH et al (2006) Analysis of sterilization effect by pulsed dielectric barrier discharge. J Electrostat 641:17–22. https://doi.org/10.1016/j.elstat.2005.04.001
5. Klämpfl TG et al (2012) Cold atmospheric air plasma sterilization against spores and other microorganisms of clinical interest. Appl Environ Microbiol 78:5077–5082. https://doi.org/10.1128/AEM.00583-12
6. Priorclave North America Inc. The Thermodynamic Realities Of Medical-Grade Autoclaves. 2013. url: https://www.priorclave.com/engb/ wp-content/uploads/sites/2/2018/08/ Is-it-Hip-to-be-Square.pdf
7. Winter J, Brandenburg R, Weltmann KD (2015) Atmospheric pressure plasma jets: an overview of devices and new directions. Plasma Sour Sci Technol. https://doi.org/10.1088/0963-0252/24/6/064001
8. Tian Y et al. (2010) Inactivation of Staphylococcus aureus and Enterococcus faecalis by a directcurrent, cold atmospheric-pressure air plasma microjet '*', pp 264–269
9. Ziuzina D et al (2013) Atmospheric cold plasma inactivation of Escherichia coli in liquid media inside a sealed package. J Appl Microbiol 114:778–787. https://doi.org/10.1111/jam.12087
10. Wang H et al (2019) Sterilizing processes and mechanisms for treatment of escherichia coli with dielectric-barrier discharge plasma. Appl Environ Microbiol 86.1:e01907-19. https://doi.org/10.1128/AEM.01907-19
11. Kogelschatz U, Eliasson B, Egli W (1997) Dielectric-barrier discharges. Principle and applications. J Phys IV France 07:C4-47-C4-66. https://doi.org/10.1051/jp4:1997405
12. Ziuzina D et al (2015) Cold plasma inactivation of bacterial biofilms and reduction of quorum sensing regulated virulence factors. PLoS ONE 10:1–21. https://doi.org/10.1371/journal.pone.0138209
13. Paolo FA et al (2017) Reduction of microbial contamination and improvement of germination of sweet basil (Ocimum basilicum L.) seeds via surface dielectric barrier discharge. J Phys D Appl Phys 50.30:305401. https://doi.org/10.1088/1361-6463/aa77c8
14. Emanuele S et al (2019) UV-VIS optical spectroscopy investigation on the kinetics of long-lived RONS produced by a surface DBD plasma source. Plasma Sour Sci Technol. https://doi.org/10.1088/1361-6595/ab3c36
15. Broadwater WT, Hoehn RC, King PH (1973) Sensitivity of Three Selected Bacterial Species to Ozone. pp 391-393. https://journals.asm.org/journal/am
16. Lunov O et al (2014) Cell death induced by ozone and various non-thermal plasmas: therapeutic perspectives and limitations. Sci Rep. https://doi.org/10.1038/srep07129
17. Niveditha A et al (2021) Application of cold plasma and ozone technology for decontamination of Escherichia coli in foods- a review. Food Control. https://doi.org/10.1016/j.foodcont.2021.108338
18. Mahfoudh A et al (2010) Inactivation of vegetative and sporulated bacteria by dry gaseous ozone. Ozone Sci Eng 32:180–198. https://doi.org/10.1080/01919511003791971
19. Dick Z, Michael S, Arkady M (2011) Effectiveness of a novel ozone-based system for the rapid high-level disinfection of health care spaces and surfaces. Am J Infect Control 39:873–879. https://doi.org/10.1016/j.ajic.2011.01.012. (**ISSN: 01966553**)
20. Pajak-Zajac MZ et al (2023) Biofilm inactivation by cold plasma Antimicrobial efficacy of in-situ plasma-generated ozone against Pseudomonas aeruginosa biofilms in drains and watersubmerged surfaces. https://doi.org/10.1101/2023.08.28.553206
21. Jin J et al (2014) Bactericidal agents produced by surface micro-discharge (SMD) plasma by controlling gas compositions. Plasma Proc Polym 11:426–436. https://doi.org/10.1002/ppap.201300173
22. Pavlovich MJ, Clark DS, Graves DB (2014) Quantification of air plasma chemistry for surface disinfection. Plasma Sour Sci Technol. https://doi.org/10.1088/0963-0252/23/6/065036
23. Schairer David O et al (2012) The potential of nitric oxide releasing therapies as antimicrobial agents. Virulence 3:271–279. https://doi.org/10.4161/viru.20328. (**ISSN: 21505608**)

24. Muhammad M (2016) Nitric oxide production by high voltage electrical discharges for medical uses: a review. Plasma Chem Plasma Process. https://doi.org/10.1007/s11090-016-9698-1

25. Yukinori S et al (2012) Plasma chemistry model of surface microdischarge in humid air and dynamics of reactive neutral species. J Phys D Appl Phys 45.42:425201. https://doi.org/10.1088/0022-3727/45/42/425201

26. De Baerdemaeker K et al (2023) Non-thermal plasma decontamination using a multi-hollow surface dielectric barrier discharge: impact of food matrix composition on bactericidal efficacy. Foods. https://doi.org/10.3390/foods12020386. (**ISSN: 2304-8158**)

27. Malik MA et al (2016) Ozone-free nitric oxide production using an atmospheric pressure surface discharge - A way to minimize nitrogen dioxide co-production. Chem Eng J 283:631–638. https://doi.org/10.1016/j.cej.2015.07.092. (**ISSN: 13858947**)

28. Vaisala. HUMICAP Handheld Humidity and Temperature Meter Series HM40. https://docs.vaisala.com/v/u/B211064EN-F/en-US

29. Manley TC (1943) The electric characteristics of the ozonator discharge. Trans Electrochem Soc 84:83–96

30. Ronny B (2017) Dielectric barrier discharges: progress on plasma sources and on the understanding of regimes and single filaments. Plasma Sou Sci Technol 26.5:053001. https://doi.org/10.1088/1361-6595/aa6426

31. Hui J et al (2013) Experimental study of Q-V Lissajous figures in nanosecond-pulse surface discharges. IEEE Trans Dielectr Electr Insul 20.4:1101–1111. https://doi.org/10.1109/TDEI.2013.6571423

32. Tetsuji S et al (2012) The dynamics of ozone generation and mode transition in air surface micro-discharge plasma at atmospheric pressure. New J Phys 14.10:103028. https://doi.org/10.1088/1367-2630/14/10/103028

33. Guennadi S, Joseleau-Petit D, Richard DA (2007) Escherichia coli physiology in Luria-Bertani broth. J Bacteriol 189.238:746–8749. https://doi.org/10.1128/JB.01368-07. (**ISSN: 00219193**)

34. Hagen SJ (2010) Exponential growth of bacteria: constant multiplication through division. Am J Phys 78.12:1290–1296. https://doi.org/10.1119/1.3483278

35. Avino F et al (2023) Surface DBD degradation in humid air, and a hybrid surface-volume DBD for robust plasma operation at high humidity. J Phys D Appl Phys 56.34:345201. https://doi.org/10.1088/1361-6463/acd2e4

36. CoStat - Software version 6.45. http://cohortsoftware.com/costat.html

37. Motulsky H (2013) Intuitive Biostatistics: A Nonmathematical Guide to Statistical Thinking. Oxford University Press, Third

38. Jin S et al (2016) Bactericidal effects against s aureus and physicochemical properties of plasma activated water stored at different temperatures. Sci Rep. https://doi.org/10.1038/srep28505

39. Bruker. Bruker VERTEX 80/80v FT-IR Spectrometers. https://www.bruker.com/en/products-and-solutions/infrared-and-raman/ft-ir-research-spectrometers/vertex-research-ft-ir-spectrometer/vertex-80-80v-ft-ir-spectrometer.html

40. Elise V et al (2023) NH3 and HNOx formation and loss in nitrogen fixation from air with water vapor by nonequilibrium plasma. ACS Sustain Chem Eng 11.10:4289–4298. https://doi.org/10.1021/acssuschemeng.3c00208

41. HITRAN on the Web. https://hitran.tsu.ru/

42. Ekspla. PL2230 series datasheet. https://ekspla.com/wp-content/uploads/products/picosecond-lasers/PL2230/Ekspla_PL2230-datasheet_-20230109.pdf

43. Teledyne Princeton Instruments. PI-MAX®4: 1024f datasheet. https://www.princetoninstruments.com/wp-content/uploads/2020/04/PIMAX4_1024f_datasheet.pdf

44. van Gessel AFH et al (2013) Temperature and NO density measurements by LIF and OES on an atmospheric pressure plasma jet. J Phys D Appl Phys 46.9:095201. https://doi.org/10.1088/0022-3727/46/9/095201

45. Uddi M et al (2009) Nitric oxide density measurements in air and air/fuel nanosecond pulse discharges by laser induced fluorescence. J Phys D Appl Phys 42.7:075205. https://doi.org/10.1088/0022-3727/42/7/075205

46. van Gessel AFH, Alards KMJ, Bruggeman PJ (2013) NO production in an RF plasma jet at atmospheric pressure. J Phys D Appl Phys 46.26:265202. https://doi.org/10.1088/0022-3727/46/26/265202

47. Brooker MH, Irish DE (1968) Infrared and Raman spectral studies of KNO2-KNO3 solutions. Can J Chem 46.2:229–233. https://doi.org/10.1139/v68-036

48. Alexandra W et al (2021) An in situ FTIR study of DBD plasma parameters for accelerated germination of arabidopsis thaliana seeds. Int J Mol Sci. https://doi.org/10.3390/ijms222111540. (**ISSN: 1422-0067**)

49. Haiqiang W et al (2016) Numerical evaluation of the effectiveness of NO2 and N2O5 generation during the NO ozonation process. J Environ Sci (China) 41:51–58. https://doi.org/10.1016/j.jes.2015.05.015. (**ISSN: 10010742**)

50. Hall Jackson R et al (2020) Mode of nitric oxide delivery affects antibacterial action. ACS Biomater Sci Eng 6:433–441. https://doi.org/10.1021/acsbiomaterials.9b01384. (**ISSN: 23739878**)

Publisher's Note Springer Nature remains neutral with regard to jurisdictional claims in published maps and institutional affiliations.